Multi-parametric MRI-based peritumoral radiomics on prediction of lymph-vascular space invasion in early-stage cervical cancer

Linpeng Cui* (ID)
Tao Yu* (ID)
Yangyang Kan (ID)
Yue Dong (ID)
Yahong Luo (ID)
Xiran Jiang (ID)

PURPOSE
This retrospective study aims to evaluate the use of multi-parametric magnetic resonance imaging (MRI) in predicting lymph-vascular space invasion (LVSI) in early-stage cervical cancer using radiomics methods.

METHODS
A total of 163 patients who underwent contrast-enhanced T1-weighted (CE T1W) and T2-weighted (T2W) MRI scans at 3.0T were enrolled between January 2014 and September 2019. Radiomics features were extracted and selected from the tumoral and peritumoral regions at different dilation distances outside the tumor. Mann–Whitney U test, the least absolute shrinkage and selection operator logistic regression, and logistic regression was applied to select the predictive features and develop the radiomics signature. Univariate analysis was performed on the clinical characteristics. The radiomics nomogram was constructed incorporating the radiomics signature and the selected important clinical predictor. Prediction performance of the radiomics signature, clinical model, and nomogram was evaluated with the area under the curve (AUC), specificity, sensitivity, calibration, and decision curve analysis (DCA).

RESULTS
A total of 5 features that were selected from the peritumoral regions with 3- and 7-mm dilation distances outside tumors in CE T1W and T2W MRI, respectively, showed optimal discriminative performance. The radiomics signature comprising the selected features was significantly associated with the LVSI status. The radiomics nomogram integrating the radiomics signature and degree of cellular differentiation exhibited the best predictability with AUCs of 0.771 (specificity (SPE) = 0.831 and sensitivity (SEN) = 0.581) in the training cohort and 0.788 (SPE = 0.727, SEN = 0.773) in the validation cohort. DCA confirmed the clinical usefulness of our model.

CONCLUSION
Our results illustrate that the radiomics nomogram based on MRI features from peritumoral regions and the degree of cellular differentiation can be used as a noninvasive tool for predicting LVSI in cervical cancer.

From the Department of Biomedical Engineering (L.C., X.J. ✉ xrjiang@cmu.edu.cn), China Medical University, Shenyang, China; Department of Radiology (T.Y., Y.K., Y.D., Y.L. ✉ luoyahong8888@hotmail.com), Cancer Hospital of China Medical University, Liaoning Cancer Hospital and Institute, Shenyang, China.

*Linpeng Cui and Tao Yu contributed equally to this work.

Cervical cancer, as the fourth common female malignancy worldwide,[1] is becoming one of the leading causes of cancer death,[2] with over 300 000 deaths worldwide per year.[3] Lymph-vascular space invasion (LVSI), including blood vessel invasion and lymphatic vessel invasion, is closely related to lymph node metastasis and distant metastasis in cervical cancer, which often lead to poor prognosis.[4] Since the 5-year survival rate for metastatic cervical cancer is only 16.5%, early diagnose of LVSI is essential in making timely therapeutic decision and improving prognosis for patients.[5] However, radiologists still cannot reliably predict the risk of LVSI through preoperative imaging due to the absence of specific imaging biomarkers.[6] Progress in magnetic resonance imaging (MRI)-based assessment of cervical cancer has been significant during the last decades.[7,8] The contrast-enhanced T1-weighted (CE T1W), T2-weighted (T2W), and diffusion-weighted imaging (DWI) MRI have been used for the prediction of LVSI in cervical cancer.[9-11] However, conventional MRI is based on subjective visual assessments and has low overall performance.[12] The main reason might be that some predictive quantitative features related to LVSI are hidden in higher dimension and can hardly be recognized through visual inspection.

In recent years, radiomics approaches have received increasing attraction due to the impressive abilities of high-throughput extraction of quantitative imaging features and the subsequent analysis using statistical methods and machine learning classifiers to develop models for tumor diagnosing, staging, and therapeutic response predicting.[13-15] Previous efforts have indicated the good potential of MRI-based radiomics in predicting lymph node metastasis,[16,17] parametrial invasion,[18] and therapeutic outcomes[19,20] in cervical cancer. These findings suggested that radiomics can contribute to revealing associations between MRI radiomics features and the underlying pathophysiology of cervical cancer. While the existing reports on MRI-based radiomics in predicting the LVSI in cervical cancer were limited and have an inherent bias with a limited number of patients and features types, a recent study revealed that CE T1W MRI could give partial information in evaluating the LVSI status.[4] Although the study was preliminary since the prediction accuracy was only 60% by the developed model with CE T1W MRI, the results were encouraging, which enlightened us on the association of MRI features with the LVSI status in cervical cancer. Another recent report assessed the values of DWI combined with DCE T1W and T2W MRI in predicting the LVSI in cervical cancer and generated AUCs ranging from 0.659 to 0.814.[21] However, the study has limitations since only 66 features were evaluated from 56 enrolled patients. Besides, the published work both focused on the tumoral regions, without considering information from peritumoral regions.

In this study, we evaluated the tumoral and peritumoral regions in the CE T1W and T2W images on predicting the LVSI status in cervical cancer and developed a fusion

Main points

- Radiomics features were extracted and analyzed from contrast-enhanced T1-weighted and T2-weighted magnetic resonance imaging for predicting lymph-vascular space invasion (LVSI) in cervical cancer.

- The LVSI prediction performance of tumoral and peritumoral regions in the 2 MRI sequences was analyzed and compared.

- The radiomics nomogram integrating the radiomics signature and degree of cellular differentiation was constructed and evaluated for potential clinical application of our radiomics model.

radiomics nomogram model for potential clinical applications.

Methods

Patients

The retrospective research was approved by the ethics committee of our hospital (No.2013010) and informed consent was waived. A total of 163 early-stage cervical cancer patients who were pathologically confirmed as having early-stage cervical cancer in the hospital from January 2014 to September 2019 were enrolled. The numbers of the patients with or without LVSI were 65 and 98, respectively. Among the 163 patients, there were 94 cases of stage IB1, 17 cases of stage IB2, 45 cases of stage IIA1, and 7 cases of stage IIA2. There were 143 cases of squamous cell carcinoma, 13 cases of adenocarcinoma, and 7 cases of adenosquamous carcinoma. All patients underwent radical hysterectomy and systemic pelvic lymphadenectomy, with the gold standard of histologic results available within 2 weeks after MRI. The inclusion criteria were: (1) having undergone surgical resection with pathological confirmation, 2) complete CE T1W and T2W imaging data being recorded within 2 weeks before the surgery, and 3) being older than 18 years. The exclusion criteria were: 1) having a history of preoperative therapy (e.g. radiotherapy), 2) being companied with other cervical or tumor disease, 3) missing MRI data or histological result, and 4) having received conization treatment. All patients were randomly divided into a training cohort and a validation cohort with a stratified sampling ratio of 2 : 1.

Magnetic resonance imaging acquisition

Preoperative MRI was performed by a radiologist with 12 years of work experience using a 3.0T scanner (Siemens Magnetom Verio) with an 8-channel array sensitivity encoding abdominal coil. The DCE MRI was performed using 0.1 mmol/kg gadolinium-diethylenetriamine penta-acetic acid as contrast media, with an injection speed of 3.0 mL/s, followed by the sagittal CE T1W scanning. The imaging protocols of CE T1W and T2W MRI are as follows: (1) sagittal CE T1W images were obtained with repetition time/echo time (TR/TE), 600/11 ms; field of view (FOV), 250 × 218 mm; the number of excitations (NEX), 2; flip angle, 150; pixels spacing, 0.390 × 0.390 mm; slice thickness, 4 mm; spacing between slices,

4.8 mm; acquisition matrix, 640-560. (2) Sagittal T2-weighted images were obtained with TR/TE, 3800/116 ms; FOV, 250 × 220 mm; NEX, 2; flip angle, 120; pixels spacing, 0.558 × 0.558 mm; slice thickness, 4 mm; spacing between slices, 4.8 mm; acquisition matrix, 448-396. Prior to the imaging, patients were asked to drink water so as to fill the bladder and placed in a supine position. The MRI scanning that covered the entire pelvis was performed approximately 20 min later so that the patients would have stable breathing during the scanning. The MRI parameters and body position were consistent for all patients.

Tumor segmentation and mask dilation

The obtained MRI images were stored in the picture archiving and communication system in a DICOM format. For each patient, the regions of interest (ROIs) covering the whole tumor were drawn along the border of the tumor slice by slice in the CE T1W and T2W images by a radiologist with 12 years of work experience using the software ITK-SNAP (version 3.6.0, www.itk-snap.org). Another senior radiologist with 15 years of experience validated all manual delineations. The delineated ROIs were stored in an NII format for further analysis. Figure 1 shows the examples of the CE T1W and T2W images and manually delineated ROIs.
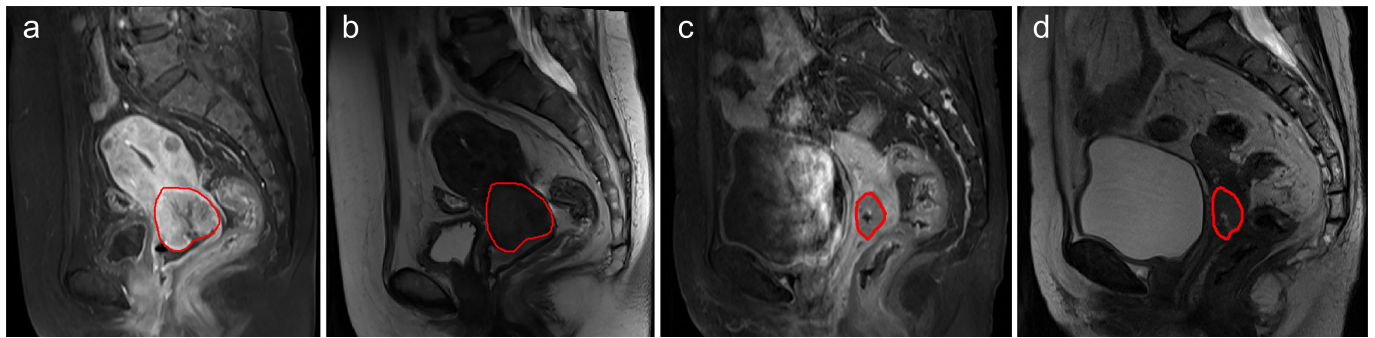
To evaluate the prediction performance of peritumoral regions, the original ROI mask was progressively enlarged with different radial distances outside the tumor at 1 mm intervals (up to a dilation distance of 10 mm) using a "SimpleITK" package in Python version 3.6. As such, 10 new masks representing different peritumoral regions were obtained for each patient. Both the tumoral and progressively enlarged peritumoral regions were used for further analysis. Figure 2 illustrated the process of the tumor region dilations.

Radiomics feature extraction

A total of 2990 radiomics features were extracted from the tumoral and peritumoral regions. The radiomics features consisted of 18 first-order statistics, 14 shape-based, and 75 texture features. The original MRI images were also filtered by wavelet, laplacian of gaussian, local binary pattern, square root, square, logarithm, exponential, gradient, and laws filters to generate transformed images. The transformed MRI images were then used

Figure 1. a-d. Examples of the magnetic resonance images used in this study. **(a)**, a contrast-enhanced T1-weighted (CE T1W) image of a cervical cancer patient without lymph-vascular space invasion (LVSI); **(b)**, a T2-weighted (T2W) image of the same patient as shown in **(a)**; **(c)**, a CE T1W image of a patient with LVSI; **(d)**, a T2W image of the same patient as shown in **(c)**. The red lines indicate the regions of interest (ROIs) drawn by radiologists.

to extract the first-order statistics and texture features. All the feature extraction and transformation process, except for laws transformation, was achieved with the Pyradiomics package (https://pyradiomics.readthedoc s.io/en/) according to a previous report.[22] To perform laws transformation, the original MRI images were filtered with 15 2-dimensional laws filters, with the 2-dimensional kernels obtained by using the calculation as follows:

$$Kernel_{i,j} = (L_i' * L_j + L_j' * L_i) / 2 \ \forall i, j = 1, 2, \cdots, 5$$

where Li and Lj represent the 5 1-dimensional kernels [L1-L5], which depict level, edge, spot, wave, and ripple texture patterns, respectively. A detailed description of the laws transformation process can be found in a previous report.[23]

Radiomics feature selection

To obtain discriminative features, first, Mann–Whitney U test was performed for each feature using the "stats" package in R language version 3.6. Features with $P < .05$ were considered as distinguishable features and retained. Afterward, the least absolute shrinkage and selection operator logistic regression was performed to eliminate irrelevant and redundant features using the "glmnet" package in R version 3.6. Third, a logistic regression model using the Akaike information criterion (AIC) as the stopping rule was performed to further select the features.

Development of the radiomics signature, clinical model, and radiomics nomogram

The radiomics signature was developed by logistic regression using the selected radiomics features weighted by corresponding logistic coefficients. A clinical model was established by logistic regression with predictive clinical characteristics
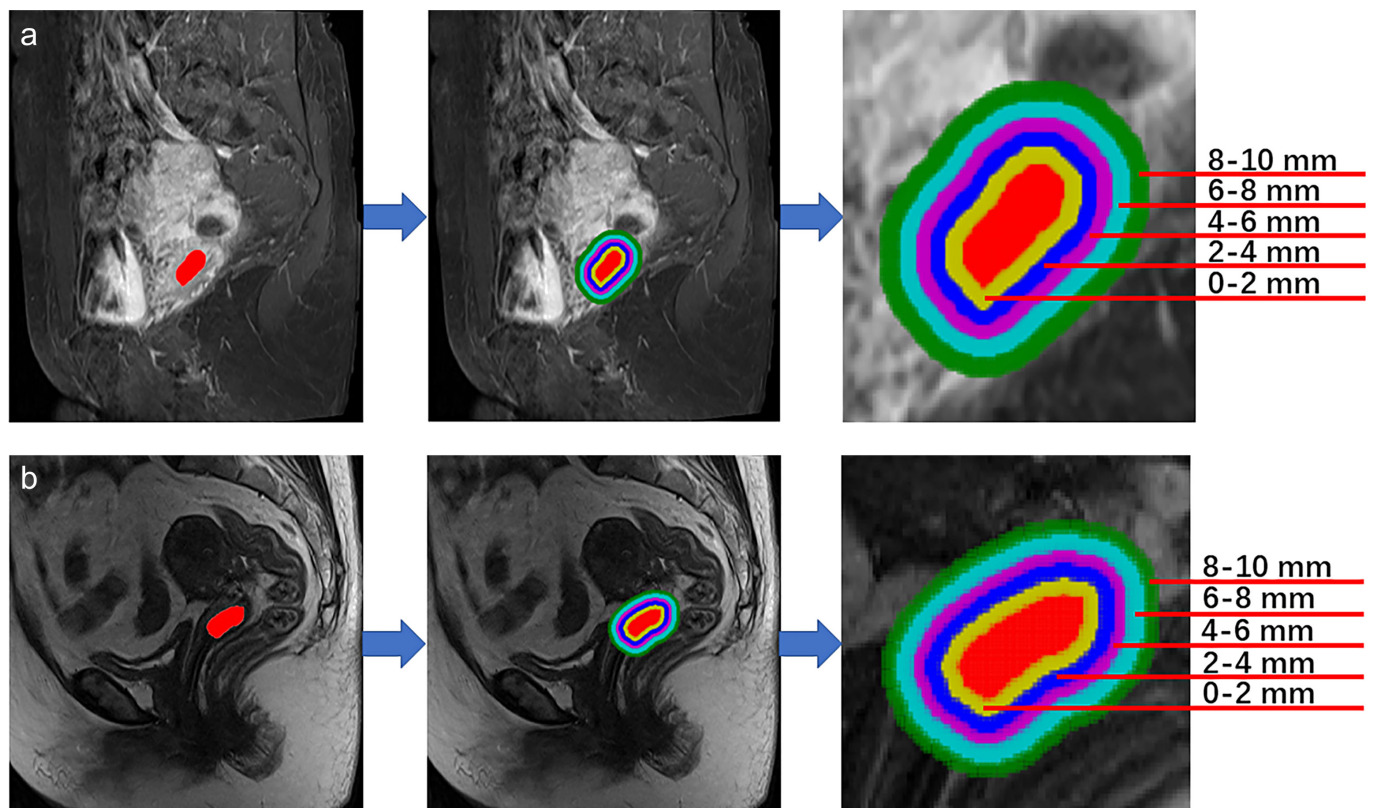
Figure 2. a-b. Examples of the dilated masks with different dilation distances on the CE T1W **(a)** and T2W **(b)** images. The red region represents the original tumor region that was segmented by radiologists. Each colorful ring indicates a 2 mm-wide dilation.
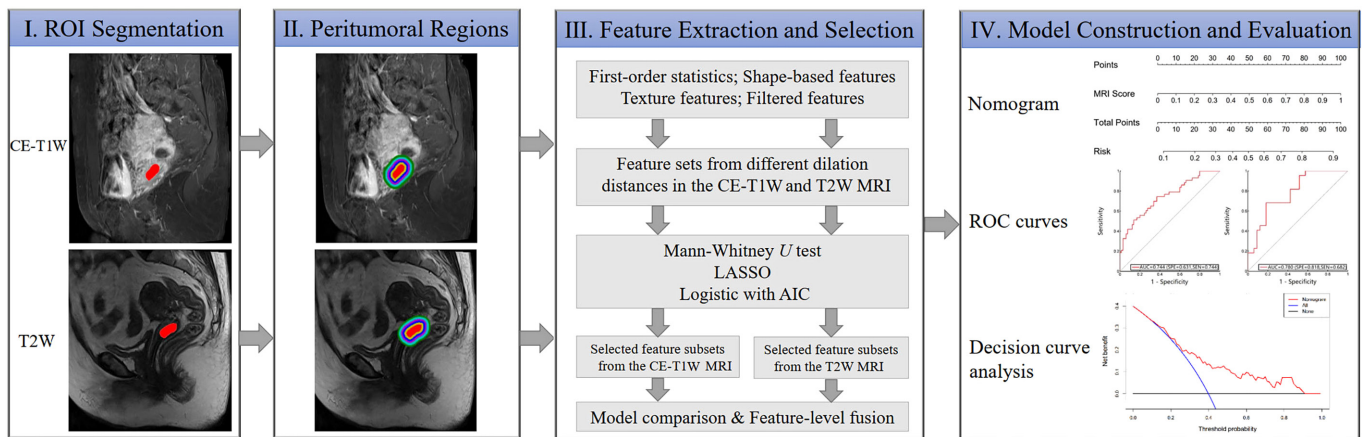
Figure 3. The work flow of this study.

($P < .05$) using the AIC as the stopping rule. An easy-to-use radiomics nomogram model was constructed integrating the radiomics signature and the important clinical predictor using "rms" package in R version 3.6 to facilitate visualization of the logistic regression model for potential clinical use.

Statistical analysis and validation strategy

Clinical characteristics including age, pregnancy, parturition, abortion, age of first intercourse, alkaline phosphatase, platelet, red blood cell, white blood cell, degree of cellular differentiation, squamous cell carcinoma antigen, federation international of gynecology and obstetrics stage, menstrual status and cancer antigen 125 were retrieved from the electronic medical records system of our hospital. Mann–Whitney U test and Chi-square test were used to evaluate the correlations between the LVSI status and clinical characteristics on continuous variables and discrete variables, respectively. $P < .05$ was

Table 1. Characteristics of cervical cancer patients in training and validation cohorts

Characteristic	Training cohort (n = 108)			Validation cohort (n = 55)		
	LVSI+	LVSI−	P	LVSI+	LVSI−	P
Age (years), mean ± SD	49.42 ± 9.16	51.11 ± 9.43	.27	52.23 ± 9.75	52.94 ± 9.03	.89
Pregnancy, n, mean ± SD	2.72 ± 1.50	2.84 ± 1.37	.58	3.63 ± 1.70	3.12 ± 1.58	.32
Parturition, n, mean ± SD	1.39 ± 0.82	1.47 ± 0.68	.45	1.72 ± 0.55	1.42 ± 0.75	.045
Abortion, n, mean ± SD	1.32 ± 1.08	1.35 ± 1.29	.81	1.90 ± 1.63	1.60 ± 1.41	.54
AFI (years), mean ± SD	22.09 ± 3.35	21.60±3.32	.57	22.45 ± 2.89	22.06 ± 4.00	.31
ALP (U/L), mean ± SD	88.90 ± 33.77	89.30 ± 24.42	.43	83.09 ± 26.48	88.78 ± 29.24	.61
PLT (10^9/L), mean ± SD	254.16 ± 53.07	258.24 ± 56.30	.73	234.86 ± 48.01	247.97 ± 59.49	.29
RBC (10^{12}/L), mean ± SD	4.45 ± 0.37	4.47 ± 0.43	.79	4.49 ± 0.35	4.48 ± 0.32	.77
WBC (10^9/L), mean ± SD	6.33 ± 1.41	6.02 ± 1.47	.34	6.21 ± 2.09	6.54 ± 1.70	.41
CA-125 (U/mL), mean ± SD	18.83 ± 9.27	23.78 ± 23.10	.75	38.26 ± 82.82	17.63 ± 12.27	.42
Degree of cellular differentiation, n (%)			.035			.15
Low	16 (37.2)	13 (20.0)		6 (27.3)	7 (21.2)	
Middle	25 (58.1)	40 (61.5)		16 (72.7)	21 (63.6)	
High	2 (4.7)	12 (18.5)		0 (0.0)	5 (15.2)	
FIGO stage, n (%)			.78			.80
IB	28 (65.1)	44 (67.7)		16 (72.7)	23 (69.7)	
IIA	15 (34.9)	21 (32.3)		6 (27.3)	10 (30.3)	
Menstrual status, n (%)			.59			.16
Menstruation	16 (37.2)	21 (32.3)		10 (45.5)	9 (27.3)	
Menopause	27 (62.8)	44 (67.7)		12 (54.5)	24 (72.7)	
SCC, n (%)			.77			.91
Normal	13 (30.2)	18 (27.7)		9 (40.9)	13 (39.4)	
Abnormal	30 (69.8)	47 (72.3)		13 (59.1)	20 (60.6)	

LVSI, lymph-vascular space invasion; SD, standard deviation; AFI, age of first intercourse; ALP, alkaline phosphatase; PLT, platelet; RBC, red blood cell; WBC, white blood cell; CA-125, cancer antigen 125; FIGO, federation international of gynecology and obstetrics; SCC, squamous cell carcinoma antigen.

considered as significant difference. All statistical hypothesis tests were 2-sided. Receiver operating characteristic curves were plotted using the "pROC" package in R version 3.6. The optimal cut-off value was obtained with the maximum Youden Index.[24] The boxplots and unsupervised cluster analysis were performed using the "ggpubr" package in R version 3.6 and the "seaborn" package in Python version 3.6, respectively. Decision curve analysis (DCA) was performed to assess the clinical usefulness of the model by calculating net benefits for a range of threshold probabilities using the "rmda" package in R version 3.6. Figure 3 depicts the overall experimental design of this study.

Results

Table 1 listed the clinical characteristics of cervical cancer patients. The degree of cellular differentiation and parturition were found to be significantly associated with the LVSI status in the training (P = .035) and validation cohort (P = .045), respectively. There was no significant difference in other characteristics between the LVSI+ and LVSI− groups in either the training or validation cohorts.

Tables 2 and 3 showed the prediction performance of the tumoral regions and progressively enlarged peritumoral regions in CE T1W and T2W MRI. The results indicated that features derived from the peritumoral regions with 3 and 7 mm dilation distances outside the tumor exhibited optimal prediction performance in CE T1W and T2W MRI, respectively.

Table 4 listed the prediction performance of the 5 most important features selected from the 3 and 7 mm dilation distances in the peritumoral regions (2 from CE T1W and 3 from T2W MRI) and the MRI signatures built based on the features.

Boxplot analysis was performed on the 5 selected features to illustrate statistical distributions of the features (Figure 4). Of the 5 features, 2 showed statistically significant differences in both the training and validation cohorts. The results showed that the values of log-sigma-5-0-mm-3D_gldm_Depen

denceVariance, original_firstorder_Kurtosis, wavelet-LHH_firstorder_Median and laws-L5W5_gldm_SmallDependenceHighGrayLevelEmphasis in the LVSI+ group tend to be larger than those in the LVSI− group. The values of original_glrlm_LongRunLowGrayLevelEmphasis tend to be smaller in the LVSI+ group than those in the LVSI− group.

Unsupervised cluster analysis was performed and depicted in Figure 5 to show the similarity and affinity between the samples. Among the 5 features, the f1 (T1-log-sigma-5-0-mm-3D_gldm_DependenceVariance) showed obvious clusters that had different values for the LVSI+ and LVSI− groups.

The radiomics signature was developed with the 5 selected imaging features and shown as follows:

Radiomics signature = −0.5285 + 0.5194 × T1-log-sigma-5-0-mm-3D_gldm_DependenceVariance + 0.3972×T1-original_firstorder_Kurtosis − 0.2291 × original_glrlm_LongRunLowGrayLevelEmphasis + 0.5680 × T2-wavelet-LHH_firstorder_Median + 0.4742 × T2-laws-L5W5_gldm_SmallDependenceHighGrayLevelEmphasis

The degree of cellular differentiation was selected as the most important predictor by the logistic regression with the smallest AIC value. The LVSI risk score was developed by integrating the radiomics signature and the degree of cellular differentiation and shown as follows:

LVSI risk score = −0.5755 × Degree of cellular differentiation + Radiomics signature

A radiomics nomogram based on the LVSI risk score was then constructed as shown in Figure 6a. The values of predictors (radiomics signature and degree of cellular differentiation) which were mapped to the points axis can be transformed into risk points. Then the sum of risk points of predictors in the total points axis can be mapped to the LVSI risk axis to obtain the probability of LVSI. The calibration curves of the radiomics nomogram showed good agreements between the actual outcomes and the nomogram-estimated probabilities in the training and validation cohorts (Figure 6b, 6c). As shown in Figure 6d and 6e, the nomogram exhibited better forecasting ability compared with the radiomics signature and the clinical model (AUCs in the training cohort, nomogram

Table 2. LVSI prediction performance of tumoral and peritumoral regions in CE T1W MRI

Dilation distances	Number of features	Cohorts	AUC	ACC	SEN	SPE
0 mm	7	Training cohort	0.820	0.796	0.651	0.908
		Validation cohort	0.577	0.600	0.636	0.576
1 mm	3	Training cohort	0.769	0.731	0.535	0.908
		Validation cohort	0.649	0.727	0.455	0.909
2 mm	3	Training cohort	0.738	0.713	0.442	0.954
		Validation cohort	0.700	0.673	0.545	0.848
3 mm*	2*	Training cohort	0.713	0.704	0.488	0.862
		Validation cohort	0.758	0.673	0.818	0.667
4 mm	4	Training cohort	0.761	0.704	0.535	0.862
		Validation cohort	0.680	0.600	0.955	0.455
5 mm	7	Training cohort	0.793	0.704	0.907	0.569
		Validation cohort	0.687	0.673	0.591	0.758
6 mm	8	Training cohort	0.816	0.796	0.814	0.723
		Validation cohort	0.581	0.600	1.000	0.212
7 mm	8	Training cohort	0.827	0.833	0.814	0.738
		Validation cohort	0.634	0.691	0.409	0.818
8 mm	9	Training cohort	0.844	0.796	0.651	0.908
		Validation cohort	0.587	0.545	1.000	0.242
9 mm	4	Training cohort	0.778	0.722	0.721	0.723
		Validation cohort	0.551	0.545	0.773	0.394
10 mm	4	Training cohort	0.764	0.722	0.605	0.831
		Validation cohort	0.496	0.491	0.909	0.273

0 mm, tumoral region; 1-10 mm, peritumoral regions.
LVSI, lymph-vascular space invasion; CE T1W, contrast-enhanced T1-weighted; AUC, area under the ROC curve; ACC, accuracy; SEN, sensitivity; SPE, specificity.
*Best model with low over-fitting and high AUC values for each sequence.

Table 3. LVSI prediction performance of tumoral and peritumoral regions in T2W MRI

Dilation distances	Number of features	Cohorts	AUC	ACC	SEN	SPE
0 mm	4	Training cohort	0.764	0.722	0.651	0.800
		Validation cohort	0.567	0.527	0.818	0.424
1 mm	5	Training cohort	0.784	0.731	0.791	0.646
		Validation cohort	0.493	0.564	0.545	0.606
2 mm	6	Training cohort	0.806	0.713	0.721	0.754
		Validation cohort	0.596	0.545	0.955	0.273
3 mm	2	Training cohort	0.737	0.676	0.907	0.477
		Validation cohort	0.627	0.636	0.455	0.879
4 mm	8	Training cohort	0.860	0.815	0.651	0.954
		Validation cohort	0.592	0.545	0.773	0.576
5 mm	5	Training cohort	0.842	0.778	0.767	0.831
		Validation cohort	0.624	0.655	0.591	0.697
6 mm	5	Training cohort	0.785	0.657	0.791	0.738
		Validation cohort	0.678	0.600	0.864	0.455
7 mm*	3*	Training cohort	0.732	0.713	0.535	0.846
		Validation cohort	0.689	0.673	0.545	0.818
8 mm	5	Training cohort	0.812	0.750	0.744	0.815
		Validation cohort	0.609	0.564	0.682	0.636
9 mm	6	Training cohort	0.796	0.722	0.814	0.692
		Validation cohort	0.426	0.600	0.500	0.545
10 mm	5	Training cohort	0.772	0.741	0.860	0.646
		Validation cohort	0.474	0.600	0.636	0.485

0 mm, tumoral region; 1-10 mm, peritumoral regions.
AUC, area under the ROC curve; ACC, accuracy; SEN, sensitivity; SPE, specificity.
* Best model with low over-fitting and high AUC values for each sequence.

Table 4. Prediction performance of the selected features and the MRI Signature

Features	Cohorts	Mean ± SD		AUC	P
		LVSI−	LVSI+		
T1-log-sigma-5-0-mm-3D_gldm_DependenceVariance (f1)	Training cohort	10.205 ± 3.835	12.717 ± 3.848	0.703	<.001
	Validation cohort	9.246 ± 3.062	11.250 ± 3.371	0.663	.043
T1-original_firstorder_Kurtosis (f2)	Training cohort	4.402 ± 1.336	5.518 ± 2.230	0.636	.017
	Validation cohort	4.037 ± 1.259	5.263 ± 1.947	0.755	.001
T2-original_glrlm_LongRunLowGrayLevelEmphasis (f3)	Training cohort	0.041 ± 0.032	0.028 ± 0.020	0.613	.047
	Validation cohort	0.049 ± 0.035	0.035 ± 0.019	0.612	.16
T2-wavelet-LHH_firstorder_Median (f4)	Training cohort	−0.017 ± 0.049	0.005 ± 0.050	0.618	.039
	Validation cohort	−0.017 ± 0.045	0.015 ± 0.065	0.612	.16
T2-laws-L5W5_gldm_SmallDependenceHighGrayLevelEmphasis (f5)	Training cohort	233.670 ± 86.805	287.558 ± 129.425	0.630	.023
	Validation cohort	220.860 ± 75.872	261.074 ± 96.774	0.618	.14
T1-3 mm MRI Signature	Training cohort	0.339 ± 0.157	0.487 ± 0.205	0.713	<.001
	Validation cohort	0.285 ± 0.122	0.424 ± 0.176	0.758	.001
T2-7 mm MRI Signature	Training cohort	0.333 ± 0.168	0.496 ± 0.199	0.732	<.001
	Validation cohort	0.295 ± 0.189	0.459 ± 0.260	0.689	.018

SD, standard deviation; LVSI, lymph-vascular space invasion; AUC, area under the ROC curve.

vs. radiomics signature vs. clinical model, 0.771 vs. 0.751 vs. 0.625; AUCs in the validation cohort, nomogram vs. radiomics signature vs. clinical model, 0.788 vs. 0.781 vs. 0.585).

Figure 7 depicted the DCA curves of nomogram, radiomics signature, and clinical model. The result showed that within most of the threshold probabilities, the nomogram had a greater net benefit than did the radiomcis signature and clinical model, which indicated that our nomogram had the best clinical utility for predicting the LVSI in cervical cancer patients.
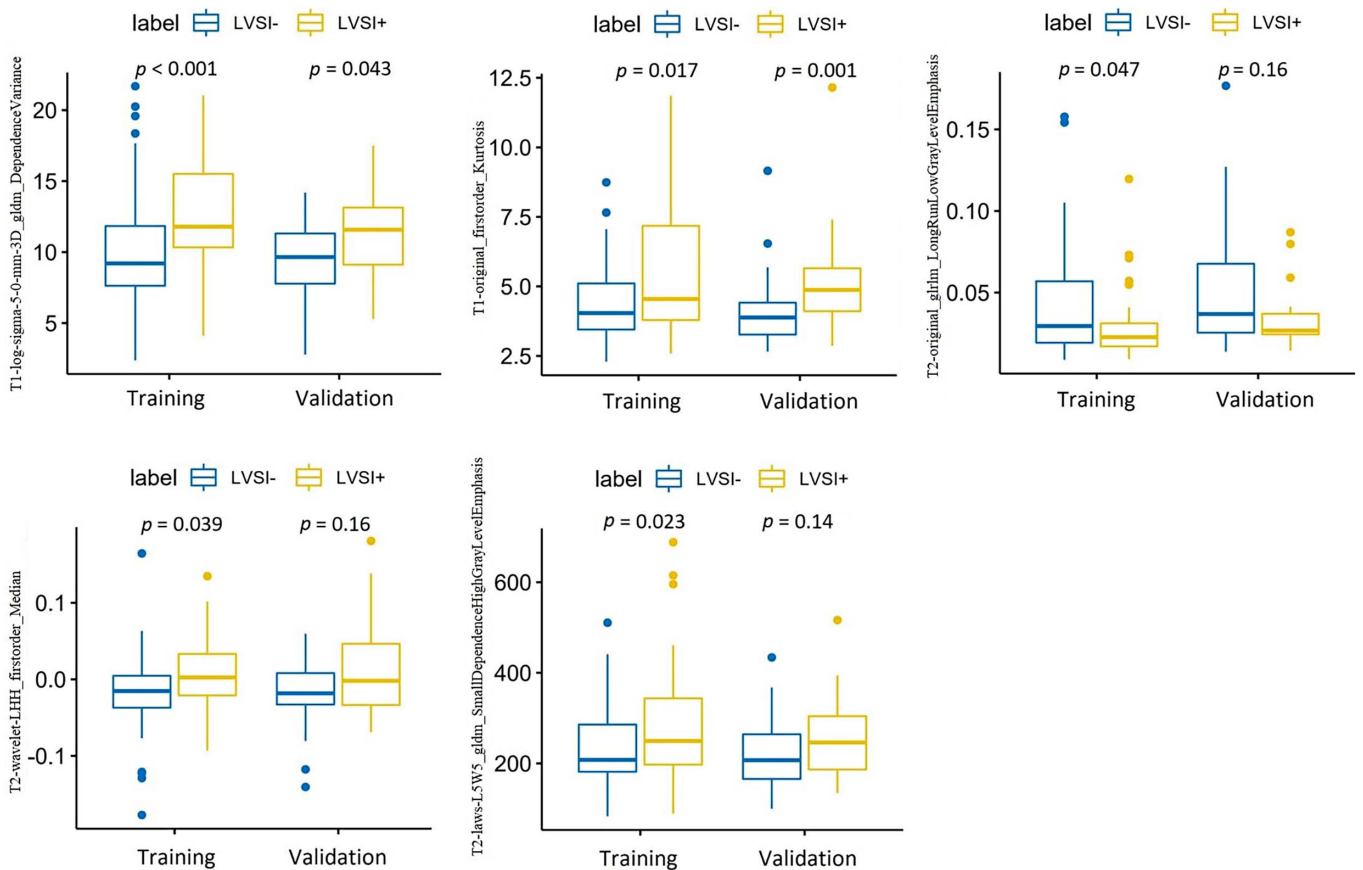
Discussion

The development of noninvasive preoperative markers for predicting the LVSI is urgent for guiding individual treatment decisions.[25] We evaluated the LVSI prediction performance of the tumoral and peritumoral regions of cervical cancer and revealed that the most predictable features can be obtained from the peritumoral regions with 3 and 7 mm dilation distances in the CE T1W and T2W image, respectively. The results can be partially explained considering the fact that tumor cells tend to migrate from the primary tumor to surrounding tissues and lead to morphological and textural changes within the peritumoral regions in medical imaging.[26-28] This phenomenon has been observed in many
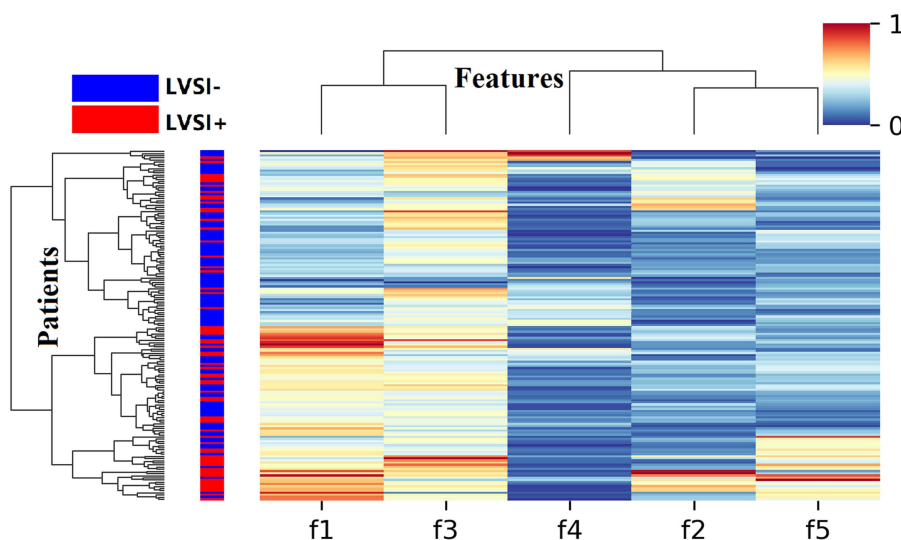
Figure 4. Boxplots of the 5 selected features from the peritumoral regions in the magnetic resonance images. Each box contains 25th and 75th quartiles and median line. $P < .05$ was considered as significantly different between the lymph-vascular space invasion (LVSI)-positive and LVSI-negative groups.

tumor diseases with discriminative power of peritumoral regions demonstrated in several recent reports.[29-31] Our results suggested that the peritumoral regions of cervical cancer may also provide important predictive information on LVSI.

We calculated 2990 radiomics features from each MRI sequence for each patient. This was far more than a recent study that only evaluated 66 features in T2 MRI from 56 patients.[21] A total of 5 features were identified as the most important predictors,

2 from CE T1W and 3 from T2W MRI. The LVSI prediction abilities of the features from the CE T1W were slightly better than those from the T2W MRI (compare AUCs and *P* values of the features from the 2 MRI sequences in Table 4). This may be partially explained considering that T2W mainly provides information on tumor morphology and stroma, while the CE T1W MRI can reflect the microenvironment and aggressiveness by showing microvascular density and perfusion,[32] which would include more information on LVSI. The T1-original_firstorder_Kurtosis feature measures the peakedness of the distribution of values in the image ROI. The higher values of this feature indicate bigger variance and greater tumor heterogeneity. Our result showed that the values of this feature were bigger in the LVSI positive group than those in the LVSI negative group, which may indicate that the probability of being LVSI tends to be higher in tumors with greater heterogeneity. The T1-log-sigma-5-0-mm-3D_gldm_DependenceVariance feature measures the variance in dependence size in the image. The sigma value (equals to 5.0) was high in this feature,

Figure 5. Cluster analysis of the 5 selected features and cervical cancer patients. The features (n = 5) were on the horizontal axis. The patients (n = 163) were on the vertical axis. The red and blue colors represent the LVSI positive and LVSI negative cervical cancer patients, respectively.
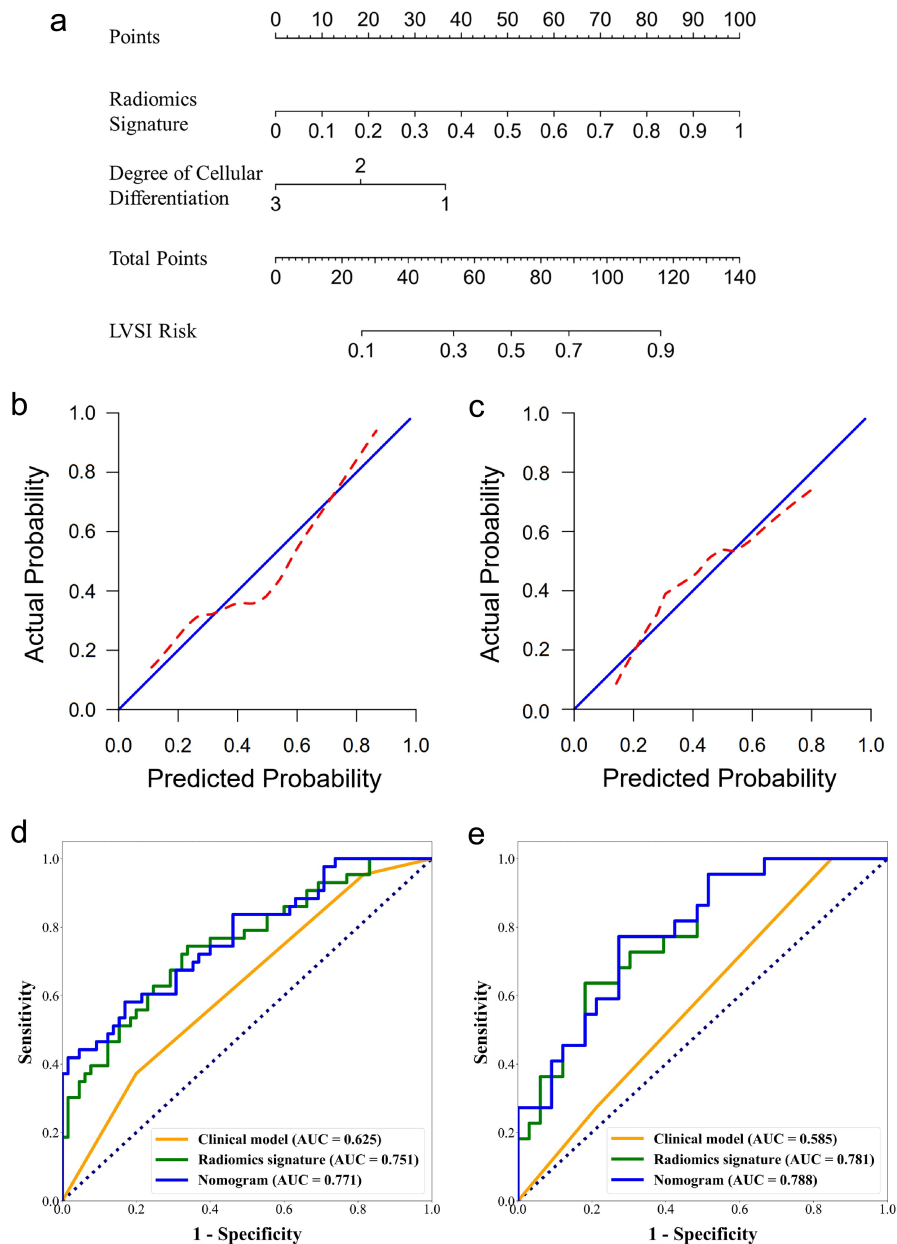
Figure 6. a-e. A radiomics nomogram integrated the radiomics signature and degree of cellular differentiation on prediction of LVSI. **(a)**, construction of the radiomics nomogram; **(b)** and **(c)**, calibration curves of the nomogram in the training and validation cohorts, respectively; **(d)** and **(e)**, receiver operating characteristic (ROC) curves of the nomogram, radiomics signature, and clinical model in the training and validation cohorts, respectively.

indicating that the model mainly focuses on coarse textures (gray level changes over a large distance) in the image since the sigma value reflects the textural coarseness. The average values of the T2-wavelet-LHH_firstorder_Median feature were bigger in the LVSI positive group, which indicates that the gray level intensity was stronger in the cervical cancer areas with LVSI positive in T2W MRI. Since the feature was derived from the peritumoral region at a 7 mm dilation distance outside the tumor, it can be partially explained considering that the tumor cells tend to migrate into peritumoral tissues

and cause changes in gray levels in the peritumoral regions in LVSI-positive patients. The result was partially similar to a previous report that suggested the wavelet filtered firstorder_Mean feature as an important predictor of LVSI in cervical cancer.[4] The T2-laws-L5W5_gldm_SmallDependenceHighGrayLevelEmphasis feature measures the joint distribution of small dependence with higher gray-level values in the image, which also indicates the important LVSI prediction value of gray level changes within peritumoral regions. Most of the identified LVSI-related features (3 of 5) belong to

high-dimensional features, which may partially explain why radiologists can hardly predict the LVSI status through unassisted examinations on preoperative MRI. All the predictive features were from peritumoral regions, which may be explainable since variations of histogram and texture characteristics in the peritumoral regions would be identified because tumor cells may disseminate through lymphatic vessels in LVSI patients.[33,34]

The radiomics signature was built with the 5 selected features and generated good prediction performance with AUCs
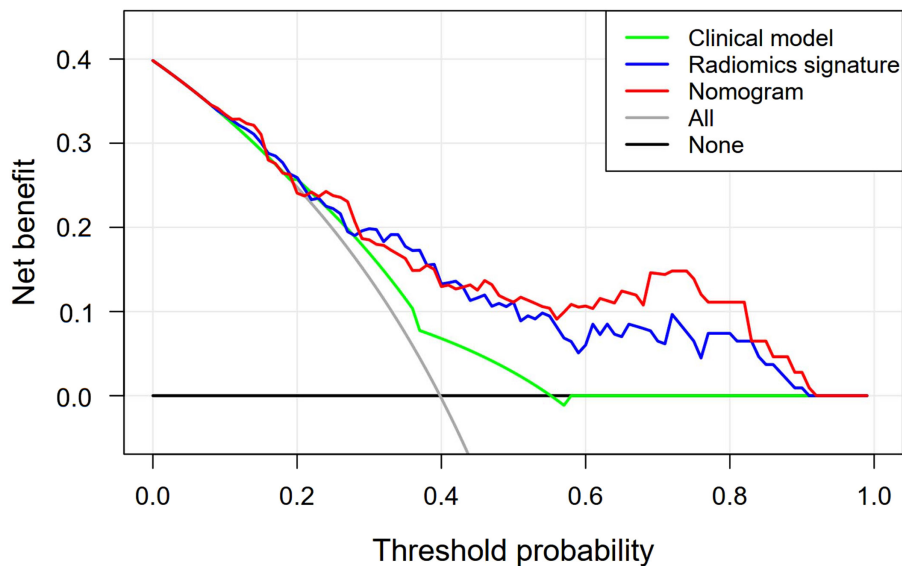
Figure 7. Decision curve analysis for the nomogram, radiomics signature and clinical model. When the threshold probability was between 0.09 and 0.92, the nomogram would be more beneficial than treating all or none of the patients. The x-axis represents threshold probability. The y-axis measures the net benefit. The red line represents our nomogram. The blue line represents radiomics signature. The green line represents the clinical model. The gray line represents the assumption that all patients were LVSI positive and treated. The black line represents the hypothesis that all patients were LVSI negative and not treated.

of 0.751 and 0.781 in the training and validation cohorts, respectively. Our results outperformed a recent work on predicting the LVSI in cervical cancer, which obtained a low prediction accuracy of 60%.[4] The main reason might be that the study only focused on the tumor region in single-sequence 1.5T MRI. On the contrary, we used 2-sequence 3.0T MRI and built models based on the peritumoral regions. We identified the degree of cellular differentiation as the most important clinical factor. This is explainable since in clinical practice, the degree of cellular differentiation negatively correlated to the degree of tumor malignancy which is one of the important factors that indicates the presence of LVSI. However, when used alone, the degree of cellular differentiation showed much lower overall performance compared with the radiomics signature.

We constructed the nomogram integrating the radiomics signature and degree of cellular differentiation and achieved the best prediction performance. The nomogram also improved net benefits across the majority of the range of threshold probabilities for cervical cancer patients. Our nomogram exhibited similar prediction AUCs compared with a recent work that described values of DWI combined with DCE T1W and T2W MRI in the prediction of LVSI based on tumoral regions, which generated AUCs ranging from 0.659 to 0.814.[21] This

may be attributed to the greater predictive power of DWI compared with the CE T1W and T2W MRI used in our study, which merits a further analysis in our future work. As a visualized model, the proposed nomogram may facilitate decision-making for clinicians without computer programing experiences. Therefore, we suggest that our nomogram can be considered as a noninvasive diagnostic tool and may contribute to early identifications of nulliparous women with early-stage cervical cancer which could be treated with more fertility-sparing operations if clinicians can preoperatively identify the LVSI.[12,35] To use our nomogram, clinicians need to identify the 3 and 7 mm peritumoral regions in the CE T1W and T2W MRI images of a patient, followed by calculating the LVSI risk score based on the proposed formula. After that, clinicians can integrate other clinical information to give a comprehensive decision on candidate medical treatments.

There are limitations to this study. First, all samples were from a single hospital. Multicenter studies would need to be conducted to enlarge the sample size. Second, correlations between the human papilloma virus (HPV) and LVSI status were missing due to the absence of complete records of HPV status in our hospital. Third, this study only used sagittal MRI, without oblique axial T2W MRI. Comparisons of the performance of sagittal and axial MRI on

the prediction of LVSI would be performed in the future. Fourth, accurate segmentation and assessment of the peritumoral regions were required since other organs such as the posterior wall or the lumen of the bladder may be included when the masks were progressively enlarged with different dilation distances, especially for the patients with FIGO stage IB2 who have a relatively large tumor with narrow peritumoral stroma. Fifth, DWI was not evaluated in this study, because the DWI was not used for routine examinations in our hospital. In addition, important serological characteristics (e.g., DLL4)[36] that were correlated with LVSI in cervical cancer were not involved in this study. In addition, the degree of cellular differentiation that integrated into the nomogram model can be obtained from preoperative cervical biopsy but not as accurate as postoperative pathological analysis. Detailed investigations about the degree of cellular differentiation will be conducted in our future work. Finally, the deep learning-based gradient-weighted class activation mapping (Grad-CAM) algorithm[37] will be applied to identify the most important peritumoral regions associated with the LVSI status.

In conclusion, our findings demonstrated that the proposed radiomics nomogram were useful predictive tools for LVSI preoperatively and noninvasively. The results may contribute to the auxiliary prediction of the possibility of LVSI in early-stage cervical cancer, which is helpful for offering timely treatments.

Conflict of interest disclosure

References

1. Barillari G, Monini P, Sgadari C, Ensoli B. The impact of human papilloma viruses, matrix metallo-proteinases and HIV protease inhibitors on the onset and progression of uterine cervix epithelial tumors: a review of preclinical and clinical studies. *Int J Mol Sci*. 2018;19(5):1418. [CrossRef]

2. Small W Jr, Bacon MA, Bajaj A, et al. Cervical cancer: a global health crisis. *Cancer*. 2017;123(13):2404-2412. [CrossRef]

3. Cohen PA, Jhingran A, Oaknin A, Denny L. Cervical cancer. *Lancet*. 2019;393(10167):169-182. [CrossRef]

4. Li Z, Li H, Wang S, et al. MR-Based Radiomics Nomogram of Cervical Cancer in Prediction of the Lymph-Vascular Space Invasion preoperatively. *J Magn Reson Imaging*. 2019;49(5):1420-1426. [CrossRef]

5. Biewenga P, van der Velden J, Mol BW, et al. Prognostic model for survival in patients with early stage cervical cancer. *Cancer*. 2011;117(4):768-776. [CrossRef]

6. Birner P, Obermair A, Schindl M, Kowalski H, Breitenecker G, Oberhuber G. Selective immunohistochemical staining of blood and lymphatic vessels reveals independent prognostic influence of blood and lymphatic vessel invasion in early-stage cervical cancer. *Clin Cancer Res*. 2001;7(1):93-97.

7. Scheidler J, Heuck AF, Steinborn M, Kimmig R, Reiser MF. Parametrial invasion in cervical carcinoma: evaluation of detection at MR imaging with fat suppression. *Radiology*. 1998;206(1):125-129. [CrossRef]

8. Sala E, Rockall A, Rangarajan D, Kubik-Huch RA. The role of dynamic contrast-enhanced and diffusion weighted magnetic resonance imaging in the female pelvis. *Eur J Radiol*. 2010;76(3):367-385. [CrossRef]

9. Mi HL, Suo ST, Cheng JJ, et al. The invasion status of lymphovascular space and lymph nodes in cervical cancer assessed by mono-exponential and bi-exponential DWI-related parameters. *Clin Radiol*. 2020;75(10):763-771. [CrossRef]

10. Downey K, Riches SF, Morgan VA, et al. Relationship between imaging biomarkers of stage I cervical cancer and poor-prognosis histologic features: quantitative histogram analysis of diffusion-weighted MR images. *AJR Am J Roentgenol*. 2013;200(2):314-320. [CrossRef]

11. Rosenkrantz AB. Histogram-based apparent diffusion coefficient analysis: an emerging tool for cervical cancer characterization? *AJR Am J Roentgenol*. 2013;200(2):311-313. [CrossRef]

12. Ai Y, Zhu H, Xie C, Jin X. Radiomics in cervical cancer: current applications and future potential. *Crit Rev Oncol Hematol*. 2020;152:102985. [CrossRef]

13. Kumar V, Gu Y, Basu S, et al. Radiomics: the process and the challenges. *Magn Reson Imaging*. 2012;30(9):1234-1248. [CrossRef]

14. Parmar C, Grossmann P, Bussink J, Lambin P, Aerts HJWL. Machine learning methods for quantitative radiomic biomarkers. *Sci Rep*. 2015;5:13087. [CrossRef]

15. Afshar P, Mohammadi A, Plataniotis KN, Oikonomou A, Benali H. From handcrafted to deep-learning-based cancer Radiomics: challenges and opportunities. *IEEE Signal Process Mag*. 2019;36(4):132-160. [CrossRef]

16. Kan Y, Dong D, Zhang Y, et al. Radiomic signature as a predictive factor for lymph node metastasis in early-stage cervical cancer. *J Magn Reson Imaging*. 2019;49(1):304-310. [CrossRef]

17. Wu Q, Wang S, Chen X, et al. Radiomics analysis of magnetic resonance imaging improves diagnostic performance of lymph node metastasis in patients with cervical cancer. *Radiother Oncol*. 2019;138:141-148. [CrossRef]

18. Wang T, Gao T, Guo H, et al. Preoperative prediction of parametrial invasion in early-stage cervical cancer with MRI-based radiomics nomogram. *Eur Radiol*. 2020;30(6):3585-3593. [CrossRef]

19. Altazi BA, Fernandez DC, Zhang GG, et al. Investigating multi-radiomic models for enhancing prediction power of cervical cancer treatment outcomes. *Phys Med*. 2018;46:180-188. [CrossRef]

20. Fang J, Zhang B, Wang S, et al. Association of Mri-derived radiomic biomarker with disease-free survival in patients with early-stage cervical cancer. *Theranostics*. 2020;10(5):2284-2292. [CrossRef]

21. Wu Q, Shi D, Dou S, et al. Radiomics analysis of multiparametric MRI evaluates the pathological features of cervical squamous cell carcinoma. *J Magn Reson Imaging*. 2019;49(4):1141-1148. [CrossRef]

22. van Griethuysen JJM, Fedorov A, Parmar C, et al. Computational radiomics system to decode the radiographic phenotype. *Cancer Res*. 2017;77(21):e104-e107. [CrossRef]

23. Wei J, Yang G, Hao X, et al. A multi-sequence and habitat-based MRI radiomics signature for preoperative prediction of MGMT promoter methylation in astrocytomas with prognostic implication. *Eur Radiol*. 2019;29(2):877-888. [CrossRef]

24. Ruopp MD, Perkins NJ, Whitcomb BW, Schisterman EF. Youden Index and optimal cut-point estimated from observations affected by a lower limit of detection. *Biom J*. 2008;50(3):419-430. [CrossRef]

25. Herr D, König J, Heilmann V, Koretz K, Kreienberg R, Kurzeder C. Prognostic impact of satellite-lymphovascular space involvement in early-stage cervical cancer. *Ann Surg Oncol*. 2009;16(1):128-132. [CrossRef]

26. Pérez-Morales J, Tunali I, Stringfield O, et al. Peritumoral and intratumoral radiomic features predict survival outcomes among patients diagnosed in lung cancer screening. *Sci Rep*. 2020;10(1):10528. [CrossRef]

27. Zhuo Y, Feng M, Yang S, et al. Radiomics nomograms of tumors and peritumoral regions for the preoperative prediction of spread through air spaces in lung adenocarcinoma. *Transl Oncol*. 2020;13(10):100820. [CrossRef]

28. Wang X, Zhao X, Li Q, et al. Can peritumoral radiomics increase the efficiency of the prediction for lymph node metastasis in clinical stage T1 lung adenocarcinoma on CT? *Eur Radiol*. 2019;29(11):6049-6058. [CrossRef]

29. Jain RK, Tong RT, Munn LL. Effect of vascular normalization by antiangiogenic therapy on interstitial hypertension, peritumor edema, and lymphatic metastasis: insights from a mathematical model. *Cancer Res*. 2007;67(6):2729-2735. [CrossRef]

30. Beig N, Khorrami M, Alilou M, et al. Perinodular and intranodular Radiomic features on lung CT images distinguish adenocarcinomas from granulomas. *Radiology*. 2019;290(3):783-792. [CrossRef]

31. Braman NM, Etesami M, Prasanna P, et al. Intratumoral and peritumoral radiomics for the pretreatment prediction of pathological complete response to neoadjuvant chemotherapy based on breast DCE-MRI. *Breast Cancer Res*. 2017;19(1):57. [CrossRef]

32. Ellingsen C, Walenta S, Hompland T, Mueller-Klieser W, Rofstad EK. The microenvironment of cervical carcinoma xenografts: associations with lymph node metastasis and its assessment by DCE-MRI. *Transl Oncol*. 2013;6(5):607-617. [CrossRef]

33. Botting SK, Fouad H, Elwell K, et al. Prognostic significance of peritumoral lymphatic vessel density and vascular endothelial growth factor receptor 3 in invasive squamous cell cervical cancer. *Transl Oncol*. 2010;3(3):170-175. [CrossRef]

34. Khunamornpong S, Lekawanvijit S, Settakorn J, Sukpan K, Suprasert P, Siriaunkgul S. Prognostic model in patients with early-stage squamous cell carcinoma of the uterine cervix: a combination of invasive margin pathological characteristics and lymphovascular space invasion. *Asian Pac J Cancer Prev*. 2013;14(11):6935-6940. [CrossRef]

35. Nick AM, Frumovitz MM, Soliman PT, Schmeler KM, Ramirez PT. Fertility sparing surgery for treatment of early-stage cervical cancer: open vs. robotic radical trachelectomy. *Gynecol Oncol*. 2012;124(2):276-280. [CrossRef]

36. Yang S, Liu Y, Xia B, et al. DLL4 as a predictor of pelvic lymph node metastasis and a novel prognostic biomarker in patients with early-stage cervical cancer. *Tumour Biol*. 2016;37(4):5063-5074. [CrossRef]

37. Selvaraju RR, Cogswell M, Das A, Vedantam R, Parikh D, Batra D. Grad-cam: visual explanations from deep networks via gradient-based localization. *Int J Comput Vis. Proc. Int. Conf. Comput Vis*. 2017;128(2):336-359. [CrossRef]